Deep Mining 2024 – P Andrieux & D Cumming-Potvin (eds)

doi:10.36487/ACG_repo/2465_65

Analysis of induced seismicity at Young-Davidson mine

Heba Khalil [a,*], Tuo Chen [b], Travis Blake [c], Andy Thomas [a], Hani S Mitri [b]

[a] *SRK Consulting, Canada*

[b] *Department of Mining and Materials Engineering, McGill University, Canada*

[c] *Alamos Gold Inc., Canada*

Abstract

As the demand for mineral resources is on the rise and mining operations continue to dig deeper at higher mining rates, the risks associated with mining-induced seismicity have substantially increased. Strong seismic events can cause rock mass and support system damage in drifts and stopes, resulting in production delays; more importantly, they may pose a hazard to the safety of mine operators. Thus the causes and risks associated with mining-induced seismicity must be investigated. This paper reports on the results of a case study at Young-Davidson (YD) mine in Canada. The YD mine is experiencing large seismic events at different mining horizons. The focus of this study is the MW2.0 events occurring in the lower mine in the depth range of 900 to 1,200 m below surface. The goal is to identify the root causes behind the large seismic events and suggest remedial strategies. The analysis of seismic source parameters and moment tensor inversion of five large seismic events helped identify the source mechanisms. In situ stress measurements previously conducted at the YD mine were analysed and used in a mine-wide numerical model that was generated with FLAC3D, taking into consideration the northeast-trending diabase dykes. The model simulates mining-induced stress distribution following the mine plan of primary and secondary stope extraction. Qualitative assessment of the safety factor, brittle shear ratio and stored strain energy, as well as comparison with seismic source location, magnitude and mechanism, helped provide an understanding of the seismic behaviour in the lower mine. The study revealed that strong seismic activities are attributed mainly to high pre-mining differential stress ($\sigma_1^0 - \sigma_3^0$) with σ_1^0 running parallel to the dykes. This leads to high differential stress build-up in the secondary stopes (ore pillars) and sill pillars, which causes predominantly compressive/shear seismic source mechanisms. The research completed by Khalil (2023) forms the basis of this paper.

Keywords: *underground mining, mining-induced seismicity, numerical modelling, moment tensor inversion*

1 Introduction

Mining-induced seismicity can be defined as the response of the rock mass to strain changes or failure of the underground structures due to stress redistribution in the mining area (Li et al. 2007). The risk associated with induced seismicity needs to be considered for the safety of mine operators and to minimise production delays. Induced seismicity is influenced by a variety of mining and geological parameters, and it is critical to analyse produced seismic events to understand the effects of these characteristics. Significant efforts have been made in developing methods to analyse microseismicity in underground mines. Manipulations of different seismic source parameters are used to get more information about seismic source and describe the resulting events. Instability indicators have also been developed to evaluate large seismicity in underground mines and understand the reasons behind them. This paper presents a case study of the Young-Davidson (YD) mine of Alamos Gold Inc. in northern Ontario, Canada. MW2.0 events have been recorded at different mining zones, starting in 2020. The large seismic events occurring in the lower mine zone, in the depth range of 900 to 1,200 m below surface, are the primary focus of this study. A mine-wide numerical model was constructed accounting for the northeast-trending diabase dykes in the studied area. Rock mass instability

* Corresponding author. Email address: geohebakhalil@gmail.com

was evaluated by the Hoek–Brown compressive safety factor (SF), brittle shear ratio and stored strain energy. Model results were compared with the location, magnitude and mechanism of the seismic source. Moment tensor inversion of five seismic events of magnitude MW2.0 that were recorded in the lower mine zone was carried out to identify the mechanisms of rock failure using ESG HSS Advanced software. This helps understand the influence of mining activities and geological structures on seismicity.

2 Focal mechanism solution

Having insight into the failure mechanisms of microseismic events in underground mines is critical for hazard assessment. Moment tensor inversion is commonly used to understand the source mechanisms. A previous study performed moment tensor inversion on three major events that occurred in YD mine and the focal mechanism was consistent with the mining sequence (Khalil et al. 2022). The moment tensor represents the deformations at the source based on generalised force couples arranged in a symmetrical 3 × 3 matrix (Equation 1). It represents the strength of a seismic source in terms of its seismic moment and the seismic waves radiation pattern (Dahm & Krüger 2014; Eyre & Van Der Baan 2015).

$$M = \begin{bmatrix} m_{11} & m_{12} & m_{13} \\ m_{21} & m_{22} & m_{23} \\ m_{31} & m_{32} & m_{33} \end{bmatrix} \quad (1)$$

Moment tensors are frequently displayed as beachballs since it is difficult to interpret a matrix of numbers. The beachball diagrams are stereographic projections that separate the area around the fault into four quadrants, two black and two white, divided by great-circle arcs orientated 90 degrees apart and representing the two nodal planes. P-wave motion around the source drove the particles in the black quadrants to move away from the source (P-wave first motion is upward on a seismograph) and vice versa (Figure 1). The slip direction will be from the white to the black quadrant along the fault surface (Cronin 2004).

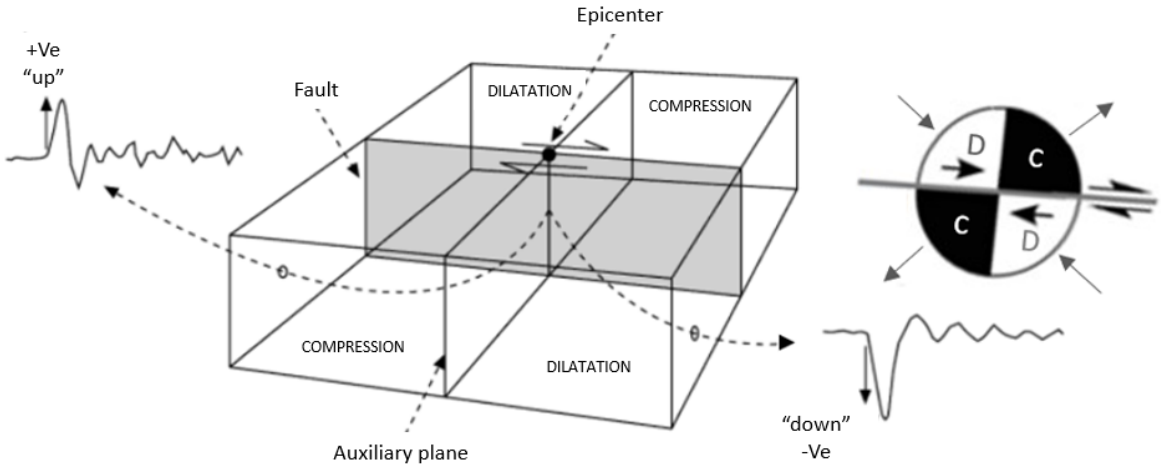

Figure 1 First motion analysis for focal mechanism solution (after Stein & Wysession 2009)

Double-couple source which represents shear failure is the most common type of moment tensor, however, research in the source mechanisms of induced seismicity shows that seismic sources usually display moment tensors with substantial non-double-couple components (Julian et al. 1998; McGarr 1992; Šílený & Milev 2008; Lizurek & Wiejacz 2011; Stec & Drzewiecki 2012; Ma et al. 2019). Knopoff & Randall (1970) decomposed the moment tensors into isotropic (M_{ISO}) and deviatoric components. The isotropic component is the part of the tensor that depicts a uniform volume change (expansion if positive and contraction if negative). While the contraction or implosion might be explained as a confined blast or rock bulking, the expansion could be the consequence of a pillarburst, buckling or a rock ejecting into space (Ma et al. 2019; Malovichko et al. 2012). The deviatoric component represents displacement with zero volume change (e.g. fault dislocation) and it can be divided into the double-couple (M_{DC}) component which represents pure

shear and the compensated linear vector dipole (M_{CLVD}) component which represent normal dislocation. The CLVD should be analysed with caution since it could be explained with other possible mechanisms. For instance, pillarburst under compression can be represented by the sum of an ISO moment tensor and a CLVD moment tensor (Eaton 2008). In underground mines it is crucial to determine the non-DC source components of moment tensors to assure the safety of mining operations (Caputa et al. 2021).

Moment tensor inversion is based on the following expression:

$$U = GM \tag{2}$$

where:

M = the moment vector composed of six independent components of moment tensor.

U = the vector representing observed amplitudes at n sensors for a given event.

G = n × 6 Gree's function derivative matrix, which represents the response of the medium from the source to the sensor (Ren et al. 2021; Dahm & Krüger 2014; Tierney 2019).

When solving the expression U = GM, the least-square method (Equation 3) is often used for calculating the moment tensor (Ren et al. 2021).

$$M = (G^T G)^{-1} G^T U \tag{3}$$

3 Numerical modelling

Numerical simulation analysis has become affordable and is crucial for analysing the behaviour of rock damage brought on by stress redistribution and blasting activities in underground mines (Chen et al. 2017; Yang et al. 2015). It can be used to determine whether a sill pillar in a tabular orebody has the potential to undergo rockburst (Castro et al. 2012). Different instability indicators can be used to investigate the potential of different failure modes (Shnorhokian et al. 2015; Heidarzadeh et al. 2019). Three instability indicators have been used in the present study to examine the modelling results: compressive stress Factor of Safety, brittle shear ratio (BSR) and burst potential index (BPI).

If the mining zone is under compression the potential for compressional/shear failure can be evaluated using the Hoek–Brown SF. It can be determined by dividing the value of Hoek–Brown maximum principal stress at failure (Hoek et al. 2002) by the maximum principal induced stress (Heidarzadeh et al. 2020). A more realistic estimate of the SF can be obtained by calculating strength and applied stress from the hydrostatic line where $\sigma_1 = \sigma_3$. In the present analysis it is simplified by subtracting the value of the minimum principal induced stress from the Hoek–Brown maximum principal stress at failure and from the maximum principal induced stress at each zone in the model as follows:

$$SF = \frac{\left[\sigma_3 + \sigma_{ci}\left(m_b \frac{\sigma_3}{\sigma_{ci}} + s\right)^a\right] - \sigma_3}{\sigma_1 - \sigma_3} \tag{4}$$

where:

m_b, s and a = rock mass material constants.

σ_{ci} = uniaxial compressive strength of the intact rock material.

σ_1 and σ_3 = major and minor principal induced stresses.

Castro et al. (2012) proposed the BSR, which is also used to assess the strainburst potential in underground mines. This ratio has been used for this purpose in a number of studies, e.g. Heidarzadeh et al. (2020; Shnorhokian et al. (2015); Vennes et al. (2020); Sainoki et al. (2021). The BSR is defined as the ratio of the differential stress to the uniaxial compressive strength (UCS) of a rock mass (Equation 5). Thus, the change in BSR reveals how the differential stress of each zone varies with mining progress. The ranges of BSR were defined along with the rock mass damage level by Castro et al. (2012) (Table 1). According to Castro et al.

(2012), when the BSR exceeds 0.7 the zone is predicted to undergo major seismic activity and is more likely to fail. Damage is initiated when BSR is between 0.3 and 0.4 in hard rock mines.

$$BSR = \frac{\sigma_1 - \sigma_3}{UCS_{int}} \quad (5)$$

Table 1 Level of rock mass damage based on brittle shear ratio (after Castro et al. 2012)

BSR	Rock mass damage	Potential of strainburst
0.35	No to minor	No
0.35–0.45	Minor (e.g. surface spalling)	No
0.45–0.6	Moderate (e.g. breakout formation)	Minor
0.6–0.7	Moderate to major	Moderate
> 0.7	Major	Major

The BPI was developed to evaluate the pillar or faceburst potential based on the amount of strain energy accumulated in the rock due to mining operations (Mitri et al. 1999). BPI relates the energy storage rate of the rock (ESR), the total energy stored in the rock mass due to mining, to its critical strain energy (e_c), the maximum strain energy the rock mass can withstand before failure (Equation 6). A BPI of 100% initially denotes a high risk of strainburst.

$$BPI = \frac{ESR}{e_c} \quad (6)$$

If the model is loaded with a stress initialisation method, the ESR at each zone can be calculated as follows:

$$ESR = \int \{\sigma\}\, d\varepsilon = \frac{1}{2}\{\varepsilon\}^T [D]\{\varepsilon\} + \{\varepsilon\}^T \{\sigma^o\} \quad (7)$$

where:

σ and ε = induced stress and strain.

σ^o = in situ stress.

[D] = elasticity matrix.

In 2D applications, Mitri et al. (1999) proposed that e_c can be evaluated from the elastic energy stored in a uniaxially loaded rock sample to the point of peak strength. For 3D applications, Vennes et al. (2020) proposed to calculate the critical strain energy using Hoek–Brown criterion as follows:

$$e_c = \frac{1}{2E}\left(\sigma_1^{peak\,2} + 2\sigma_3^2 - 2\upsilon\left(2\sigma_1^{peak}\sigma_3 + \sigma_3^2\right)\right) \quad (8)$$

where E and υ are the modulus of elasticity and Poisson's ratio, respectively.

4 Young-Davidson mine

The YD mine is situated near the community of Matachewan in Ontario, Canada. It is a gold mining operation by Alamos Gold Inc. that uses the sublevel stoping method with delayed backfill. The mine is in the gold belt known as Kirkland-Larder Lake, which hosts the world-class Kerr-Addison-Chesterville gold deposits. It is also crossed by the regional Larder Lake-Cadillac Fault Zone, which is famous for its gold camps. YD mine is hosted in a felsic intrusive syenite unit of about 1,420 m east–west by 470 m north–south. The mineralisation extends beyond 1,500 m with the orebody striking east–west. The presence of gold is mostly associated with quartz veins and scattered pyrite mineralisation within the syenite unit. The footwall predominantly consists of Timiskaming sediments (TSED) that are also observed as inter-bedded layers inside the syenite rock formation. The hanging wall is mostly composed of mafic volcanic rocks, which consist of alternating layers of mafic flows and ultramafic flows. The lithologies are intersected by diabase dykes that typically trend in a northeast direction as indicated in Figure 2 (Alamos Gold Inc. 2020). The present analysis focuses on the occurrence of seismic events with a MW2.0 in the lower mine zone with mining advance.

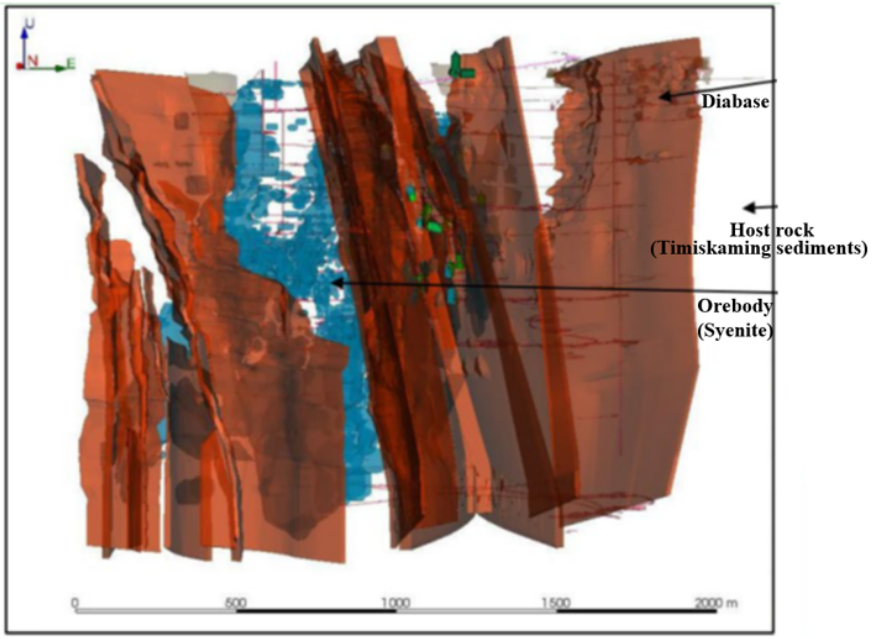

Figure 2 The three main lithology units in Young-Davidson mine (after Alamos Gold Inc. 2020)

5 Analysis of seismicity in the lower mine zone

5.1 Numerical modelling: Young-Davidson mine

5.1.1 Methodology

A mine-wide numerical model is constructed in FLAC3D, an explicit finite difference software (ITASCA 2009). The design mining geometry, surveyed stope geometry and dykes are initially fixed and simplified using Rhino 3D CAD software to produce the FLAC3D model geometry. Rhino feeds its output CAD file to Griddle$^{2.0}$, ITASCA's grid generation plug-in software, to refine and merge overlapped meshes into a conforming one. Mesh refinement is needed to generate user-defined mesh sizes. Within the regions of interest a denser mesh is used, and it gets less dense away from the orebody towards the model boundaries. Figure 3 shows the model layout.

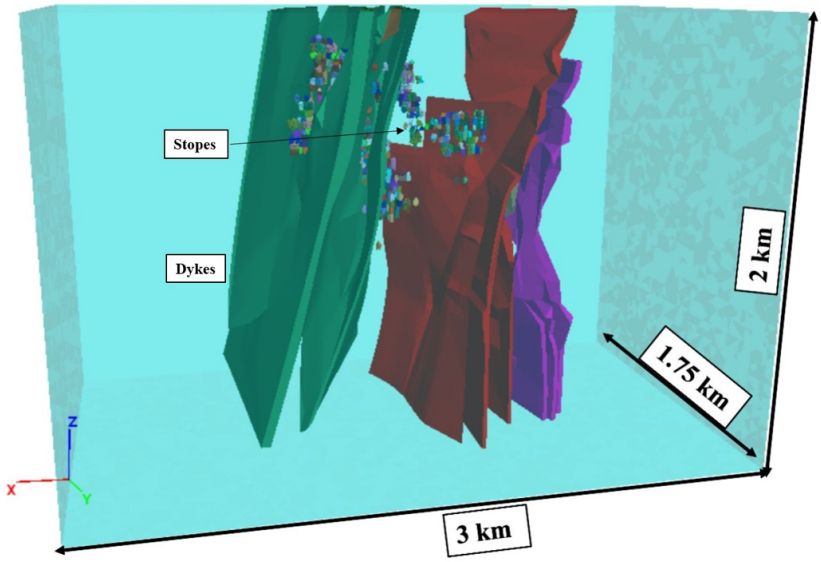

Figure 3 FLAC3D model layout

5.1.2 Mining sequence

The general sequence plan in YD mine includes three critical zones, namely stoping blocks below 9440 (lower mine zone), west mining zone 9590–9800 (upper mine and upper mid-mine zones) and the 9440–9590 central/eastern stoping blocks (lower mid-mine zone) (Alamos Gold Inc. 2020). The model includes the three zones of the mining sequence. The area of interest in this analysis is the lower mine zone from level 9440 (around 900 m) to level 9095 (1,200 m below surface). All mined stopes before the lower and lower mid-mine zones have been excavated in one step to accelerate modelling calculations. While this simplified approach leads to a slightly larger accumulation of strains due to the delayed placement of backfill, it is considered a reasonable approximation in linear elastic analysis, particularly when it is far from the area of interest. The lower mine zone is then mined step by step according to the mining sequence of the YD mine from August 2020 to April 2022, also considering the stopes mined out during this period in the lower mid-mine zone as well. Mining and backfilling are simulated in 82 stages (Figure 4).

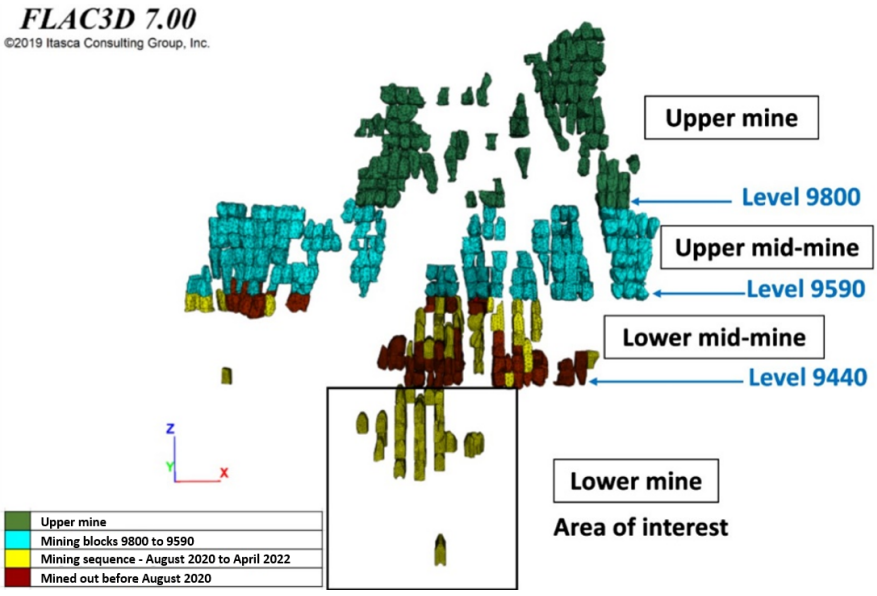

Figure 4 The general sequence at Young-Davidson mine includes three critical zones: stoping blocks below 9440, west mining zone 9590–9800 and the 9440–9590 central/eastern stoping blocks

5.1.3 Rock mass properties

To simplify model geometry, TSED, syenite, and mafic units have been combined as one material to be referred to as YD_{ave}. Table 2 presents the material properties of each domain used as the input parameters in the model (Khalil 2023).

Table 2 Average rock material properties (Khalil 2023)

Domain	UCS (MPa)	Density (kg/m^3)	Poisson's ratio	Young's modulus Er (GPa)	mb	s	a
YD_{ave}	150	2,760	0.26	40	1.61	0.0173	0.502
Diabase	175	2,980	0.24	48	1.214	0.0122	0.503
Backfill	–	1,600	0.25	0.2	–	–	–

5.1.4 In situ stress

To build a calibrated model, a series of numerical simulations was performed based on previous in situ stress measurements and estimation of in situ stress magnitude and orientation that has been done by McGill University using the diametrical core deformation technique (Li 2021; Li & Mitri 2022). Previous in situ stress measurements were conducted at YD on four levels: 9800, 9740, 9590 and 9440 (MD Eng. 2017). The in situ stress measurements indicate a high horizontal to vertical stress ratio at level 9440 which aligns with the data obtained from the nearby Macassa mine, where testing has been completed at depths greater than at YD (Alamos Gold Inc. 2020). McKinnon & Lebrie (2006) found that in the region the major principal stress is aligned 35°.

Core deformation technique was conducted on level 9130 (1,170 m) and suggests high differential stress ($\sigma_1 - \sigma_3$), which agrees with the stress measurements done on level 9440 and the in situ stress data from Macassa mine as well. It was also consistent with the stress orientation at McKinnon and Labrie. The average stress orientation from the previous measurements has been used in this study. The major principal stress was found to be trending northeast, which agrees with the regional stress orientation and core deformation analysis results. The average in situ stress values that are used in this study are as follows (Li et al. 2024).

$$\sigma_1 = -0.065\,\mathrm{X} + 677.84 \quad (9)$$

$$\sigma_2 = 0.028\,\mathrm{X} + 6.39 \quad (10)$$

$$\sigma_3 = 0.028\,\mathrm{X} - 47.72 \quad (11)$$

where X is the level number in metres based on the YD mine levels.

5.1.5 Results and discussion

5.1.5.1 Maximum compressive stress

Figure 5 shows a plan view at level 9340 representing the maximum compressive stress values around excavations mined out at stages 9, 16, 22, 33, 36, 47, 51 and 60. Note that in FLAC3D, compression is negative. The maximum principal stress is observed to be aligned with northeast–southwest direction, which compares very well with the stress measurements discussed in section 5.1.4. As a result, the maximum compressive stresses are found to reach 100 MPa at the northwest and southeast excavation corners (Mitri et al. 2000) and stress concentration zones can be observed in the transverse pillars, i.e. future secondary stopes.

The minimum principal induced stress for each model zone is retrieved by a built-in FISH-language program (ITASCA 2013) to determine if the zone is subjected to compression or tension, then the compressive SF is calculated using Equation 4. Figure 6 reveals the SF values around the excavations 9, 16, 22, 33, 36, 47, 51 and 60. SF values less than one are noticed in the zones between those excavations which may draw attention

to probability of compressional/shear failure due to stress concentration in these zones (transverse pillars) as mining advances.

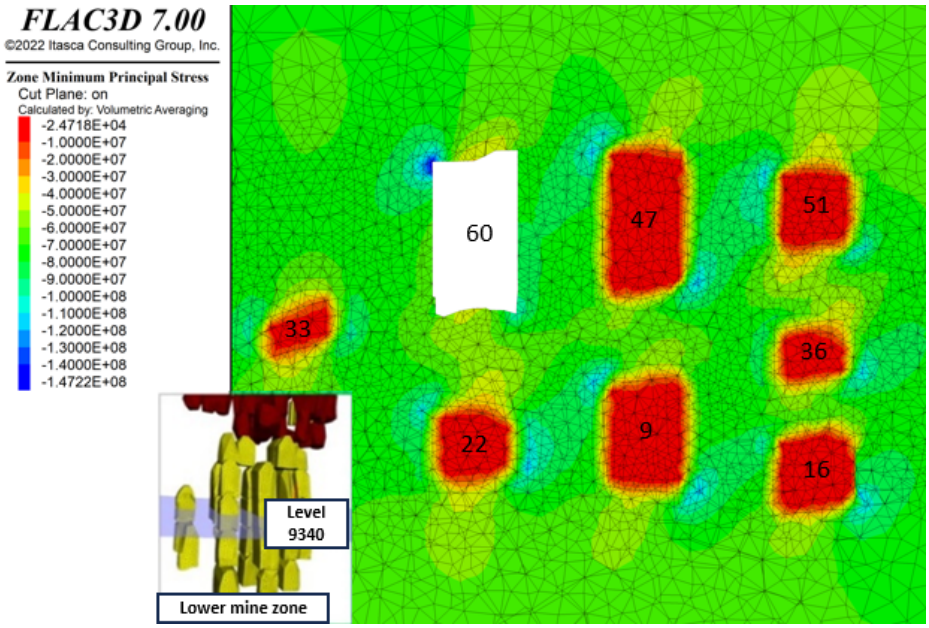

Figure 5 Plan view of level 9340 including the maximum compressive stress values around excavations mined out at stages 9, 16, 22, 33, 36, 47, 51 and 60

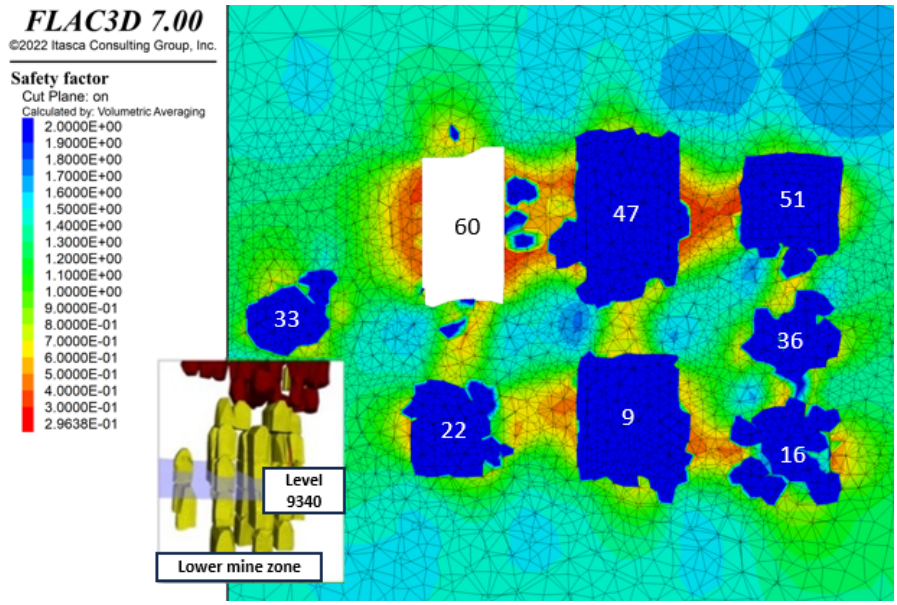

Figure 6 Safety factor values around the excavations 9, 16, 22, 33, 36, 47, 51 and 60

5.1.5.2 Brittle shear ratio

The BSR value is calculated for each model zone using Equation 5. Figure 7 shows the BSR contours obtained from the numerical model at different mining stages through level 9340. BSR values are found to align with northeast–southwest direction, and the peak values are found to be at the northwest and southeast corners of the excavations, which is consistent with the results of the maximum compressive stress. Point X is selected at the level to monitor the change in BSR value with mining sequence (the red mark on the figure). Figure 8 presents the change in BSR values at the point X with mining progress between stages 24, 33, 41, 50, 57 and 72. As mining proceeds, BSR values are found to increase from around 0.30 to 0.52, which may imply a potential of damage initiation. BSR contours are also shown for three mining stages in the pillar at level 9440

(Figure 9). Point X is selected in the centre of the pillar to examine the change in BSR value with different mining stages (24, 44, and 57). BSR values are observed to increase from around 0.33 to 0.46, which may indicate a possibility of damage initiation as well (Figure 10). Nevertheless, BSR values greater than 0.7 have been noticed in the vicinity of the excavations with mining advance, highlighting the possibility of significant rock mass damage or brittle failure.

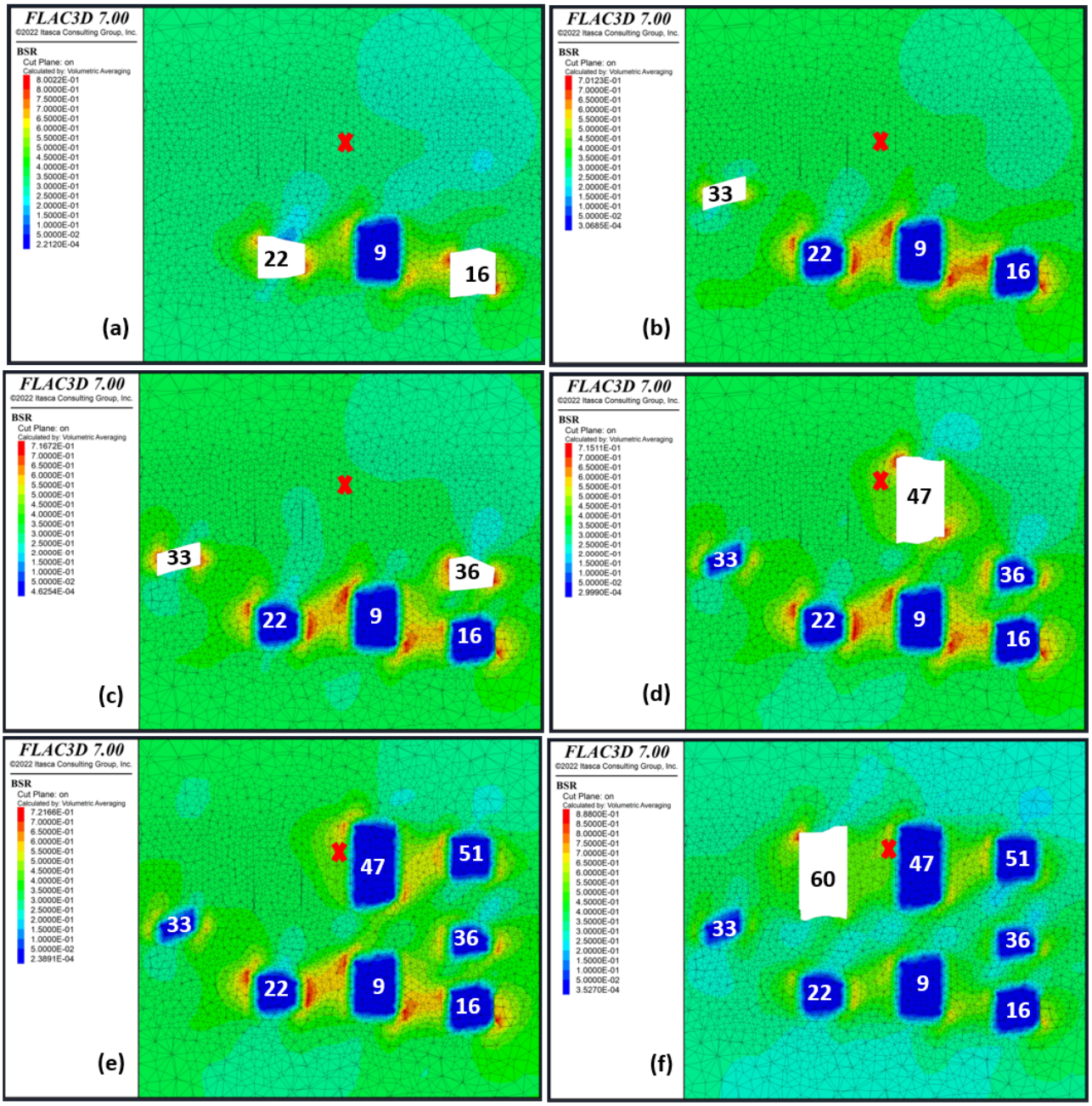

Figure 7 BSR contours on level 9340: The (a) to (f) plan views show brittle shear ratio values at mining stages 24, 33, 41, 50, 57, and 72, respectively. The numbers on the stopes represent the mining sequence

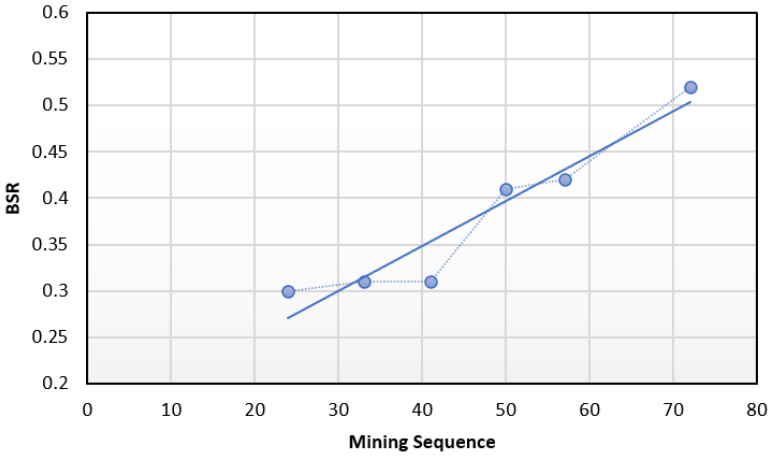

Figure 8 Change in brittle shear ratio values at point X with mining sequence at level 9340

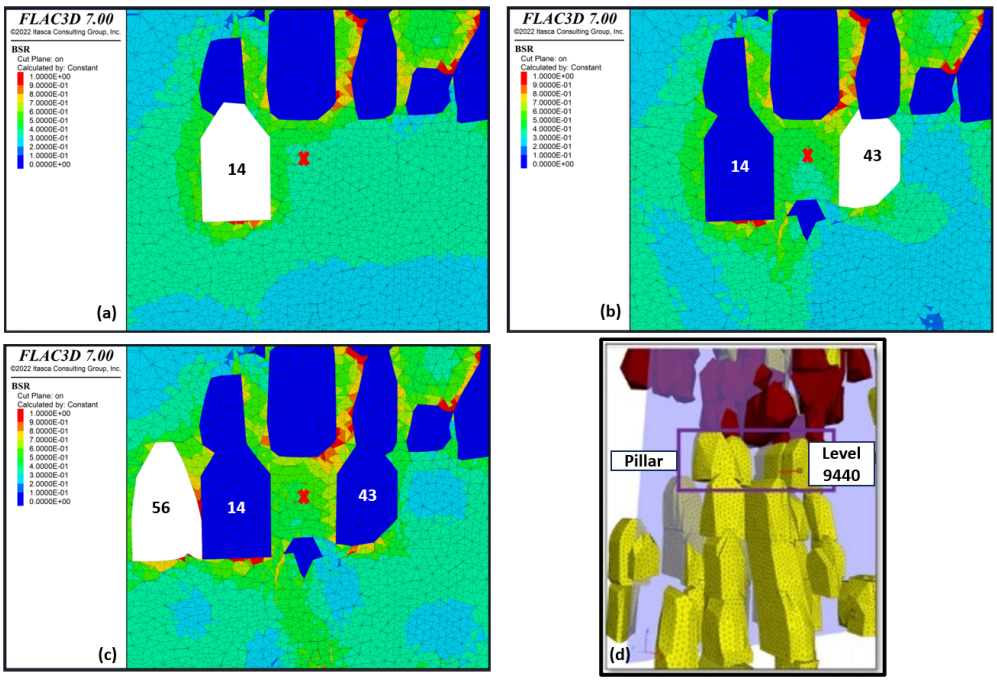

Figure 9 Brittle shear ratio contours around the pillar on level 9440: The (a) to (c) cross-sections showing BSR values at mining stages 24, 44 and 57, respectively; (d) Mining sequence through the pillar

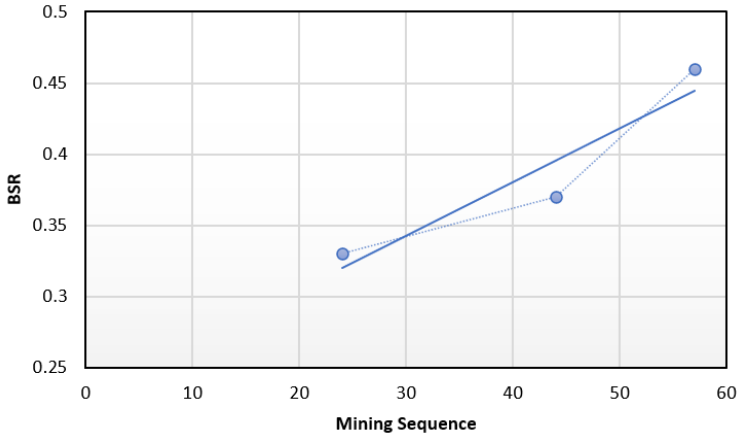

Figure 10 Change in brittle shear ratio values at point X with mining sequence through the pillar at level 9440

5.1.5.3 Burst potential index

For each zone in the model, Equations 7 and 8 are used to calculate ESR and e_c values, respectively, and then BPI value is estimated using Equation 6. BPI value is set to zero for zones in a low stress regime where $\sigma_3 < 0$ since it is only applicable to compressive zones where additional strain energy storage is expected. Figure 11 presents BPI contours around excavations at level 9340 at mining stages 24, 33, 41, 50, 57 and 72. BPI values are found to increase with mining advance and exceed 100% at different stages. High BPI at the boundaries of specific stopes may indicate the potential of local failure. BPI contours around openings 14, 43, and 56 inside the pillar at level 9440 are also presented in Figure 12. The BPI values around the openings are observed to reach 300% at stages 44 and 57. Such an increase in BPI values suggest an increase in the strain energy stored in the rock mass and in turn potential strainburst.

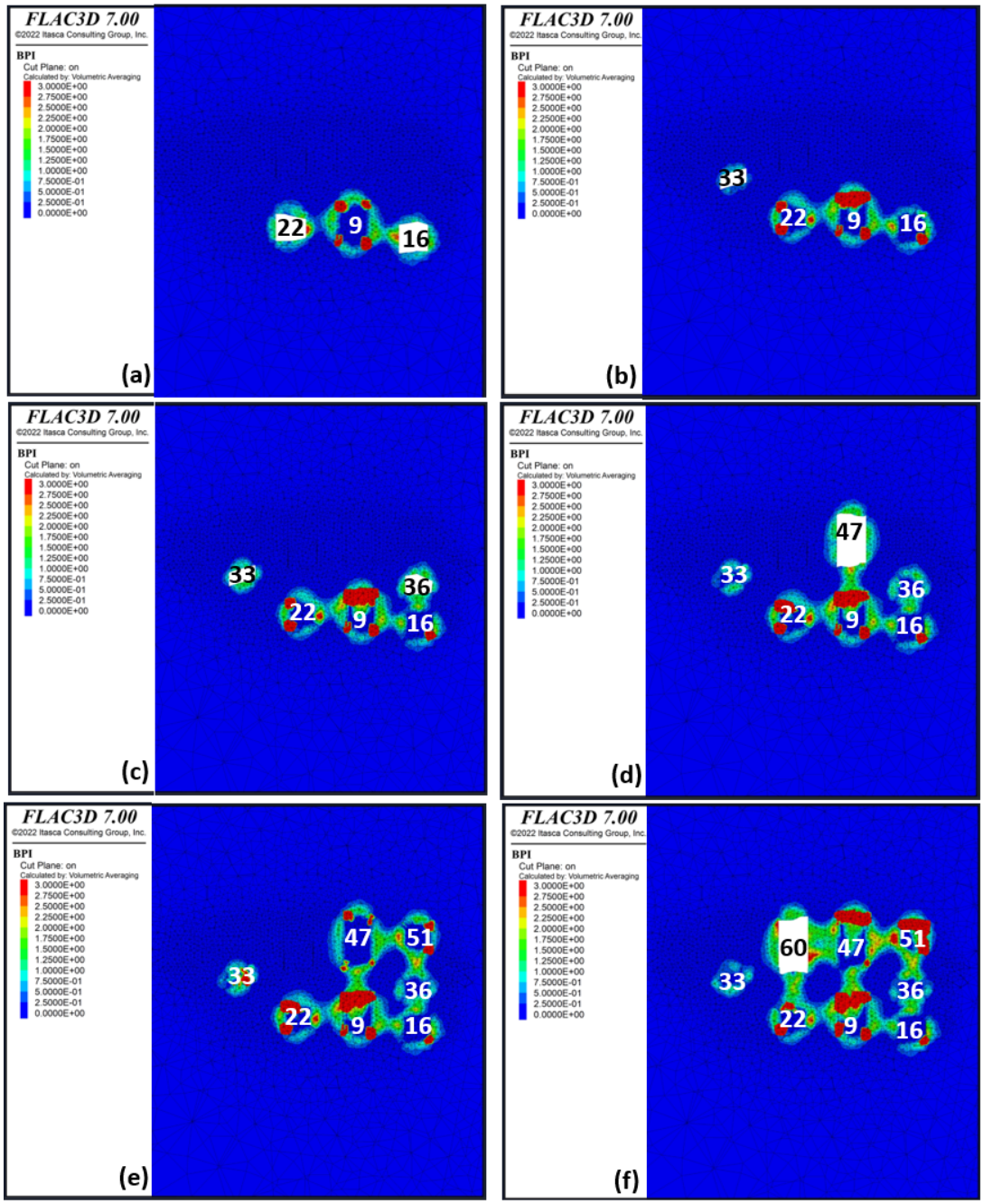

Figure 11 BPI contours on level 9340: The (a) to (f) plan views show BPI values at mining stages 24, 33, 41, 50, 57, and 72, respectively. The numbers on the stopes represent the mining sequence

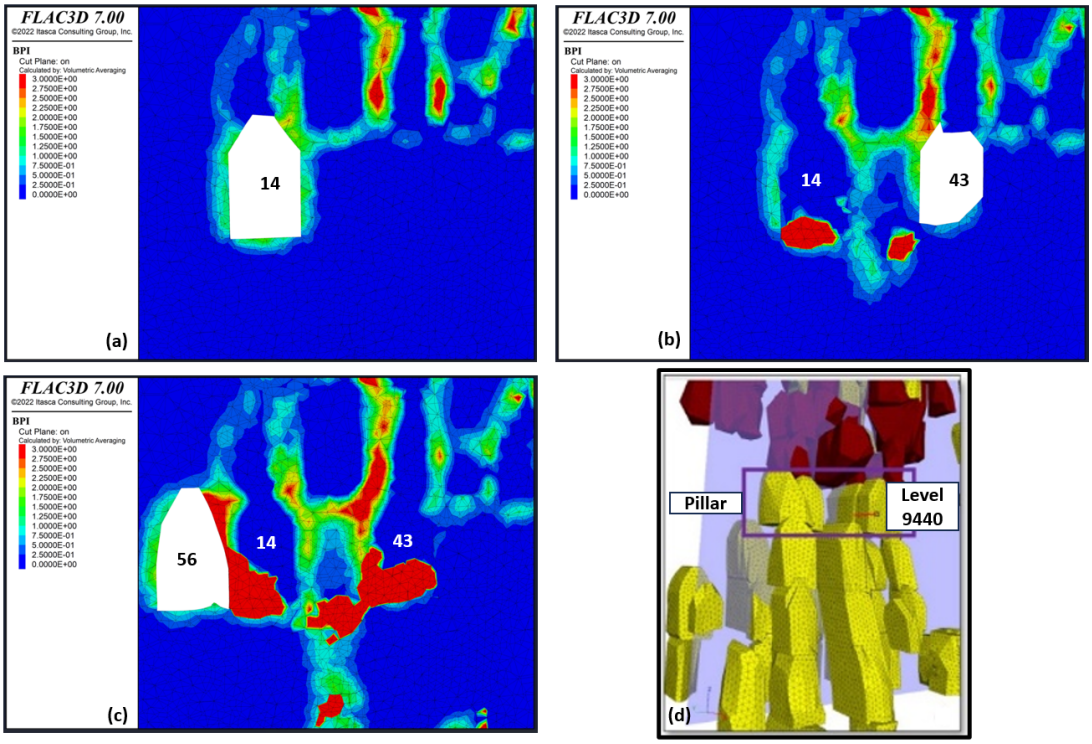

Figure 12 Burst potential index contours around the pillar on level 9440: The (a) to (c) cross-sections show burst potential index values around excavations 24, 44 and 57, respectively

5.1.5.4 Correlation between induced seismicity and instability indicators

The accuracy of seismic event location varies in YD mine, depending on the monitoring system network. Location error for the events in the study area range from 5 m to around 10 m. When rockburst indices at a point of event source are measured, the value may not be representative due to location error and model mesh quality. For instance, the source location point of a large event was estimated to be in the backfill, which is not realistic. Therefore the possible values of rockburst potential indices such as BSR, BPI and SF are obtained by searching its maximum value in a sphere with a radius of location error.

Figure 13 presents the seismic events of magnitude MW2.0 that have been observed in the deeper mine zone. To better understand the seismic behaviour in this zone, the relationship between large seismic events and the compressive SF, BSR and BPI has been analysed. Table 3 provides a summary of eight significant events with the corresponding SF, BSR and BPI values at the event locations. In accordance with the BPI, the BPI values of four large events (6 May, 30 June and 18 July 2021, and 10 February 2022) exceeded 100%, thus they could be explained by the mechanism of strainburst. The BPI of the large event that occurred on 10 February 2022 reached 930% at modelling stage 71. While this unusually high value could be due to localized poor quality meshing, it nevertheless reflects high strain energy accumulation. The compressive SF correlates with those results since the SF values are less than one (0.2 to 0.3) for those four events. SF value is also less than one (0.9) for the event of 16 October 2021. According to BSR, the values at the locations of the large seismic events are between 0.3 to 1.1. BSR values exceed the failure limit of 0.7 for the seismic events of 18 July 2021 and 10 February 2022, indicating strong strainburst potential. The BSR values for the events on 6 May and 30 June 2021 are also high, with a value of 0.6.

The instability indicators show a strong correlation with four of the eight large seismic events. However, there is no apparent correlation between all large events and the instability indicators. This could be attributed to the continuum modelling approach adopted in the study. The model treats the rock mass as a homogenous, isotropic material. This type of modelling would not capture the effect of slip along discontinuities in the ore blocks. It can be concluded that the primary cause for the strong seismic activity is slip along the structures

running parallel to the major principal stress in the northeast–southwest direction. Such slip is caused by the high deviatoric stress. However, this is yet to be confirmed with the seismic source analysis.

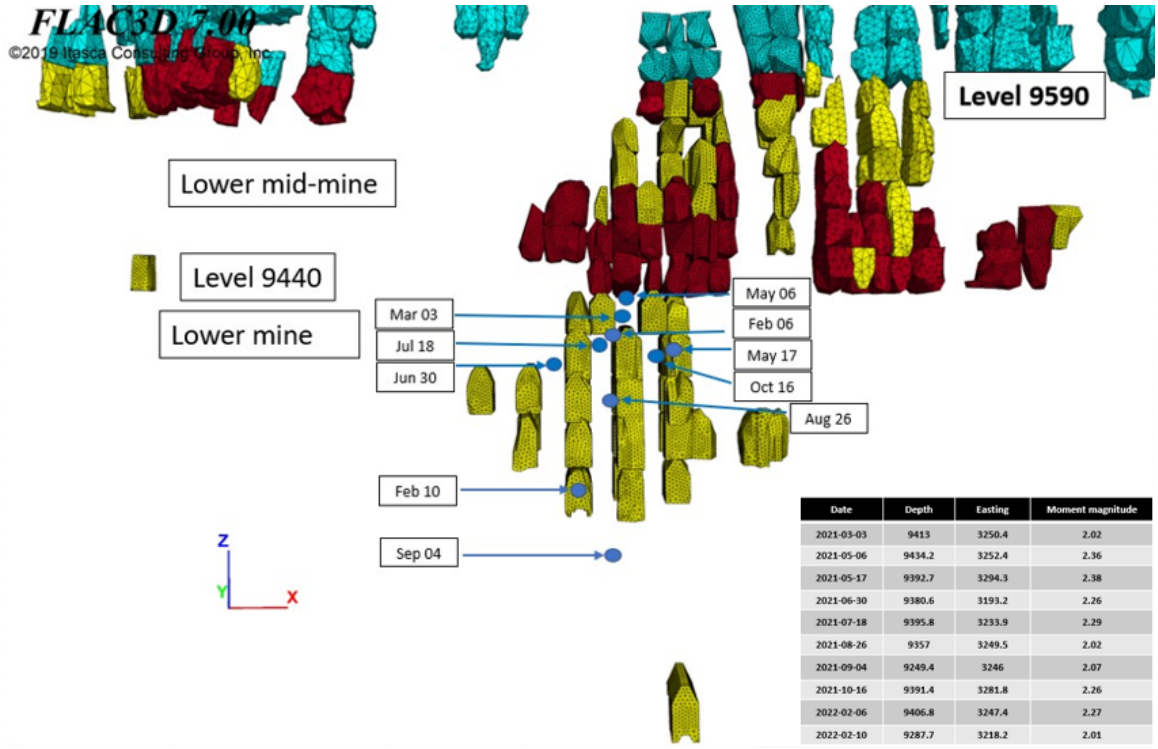

Figure 13 Seismic events of magnitude MW2.0 in the lower mine zone

Table 3 Large events in the lower mine zone with corresponding safety factor (SF), brittle shear ratio (BSR) and burst potential index (BPI) at the event locations

Event	MW	Depth–easting	SF	BSR	BPI
03/03/2021	2.02	9413–3250	1.5	0.3	0.06
06/05/2021	2.36	9434–3252	0.3	0.6	4.63
17/05/2021	2.39	9393–3294	1.4	0.3	0.01
30/06/2021	2.27	9381–3193	0.3	0.6	4.94
18/07/2021	2.30	9396–3234	0.2	1.0	6.74
04/09/2021	2.07	9249–3246	1.3	0.3	0.01
16/10/2021	2.27	9391–3282	0.9	0.4	0.23
10/02/2022	2.02	9288–3218	0.3	1.1	9.3

5.2 Moment tensor inversion

5.2.1 Methodology

To understand the root causes behind the large events, seismic moment tensor inversion (SMTI) is conducted for five large events using ESG HSS Advanced software (ESG Solutions 2020). Focal mechanism solution results of each event decompose the seismic MT into its ISO, DC and CLVD components. ESG Solutions uses the SMTI package to simulate the radiation pattern of body waves using the amplitudes of the low frequency spectral plateaus of the Brune (1970, 1971) source model and first motion polarities. A homogenous velocity model is used in the analysis, where V_p = 6,020 m/s and V_s = 3,240 m/s and. The first arrival times were

manually picked from the available records for each studied event, then all available signals were modelled separately. The amplitude spectrum of a selected seismic signal is fitted by the Brune (1970) model.

5.2.2 Results and discussion

The MT decompositions for the five events are represented in Table 4 and the graphical representations of the moment tensors are shown in Figure 14. MT decompositions reveal that for the analysed events, the percentage of the DC component is higher than 50%, suggesting that the shear failure is prevalent in those events. The high DC component aligns with the suggestion that these occurrences may be generated by slippage on structural discontinuities that run parallel to sigma 1 inside the orebody. As the continuum model shows high shear (deviatoric) stress and high BPI, it is believed that the strong seismicity is caused by sudden shear slip on the discontinuities. The negative ISO components, on the other hand, show that these sources have experienced implosive deformation, which is a core feature of compressional failure. These events are likely relevant to collapse because they also exhibit negative CLVD contributions. The source mechanisms of the five events are very close, and it is most probably shear failure/compressional failure. In regard to the locations and times of those events, it is worth noting that the analysed events happened while mining was proceeding towards the pillar, which would explain the failure mechanism.

Table 4 Moment tensor decompositions and source mechanisms reported for five events of magnitude MW2.0 in the lower mine zone

Event	ISO%	DC%	CLVD%	Failure mechanism
03/03/2021	−19.2	70.4	−10.5	Shear failure/compressional failure
06/05/2021	−20.6	61.7	−17.7	Shear failure/compressional failure
18/07/2021	−23.5	60.7	−15.8	Shear failure/compressional failure
16/10/2021	−15.2	67.8	−17	Shear failure/compressional failure
06/02/2022	−11.1	73.1	−15.7	Shear failure/compressional failure

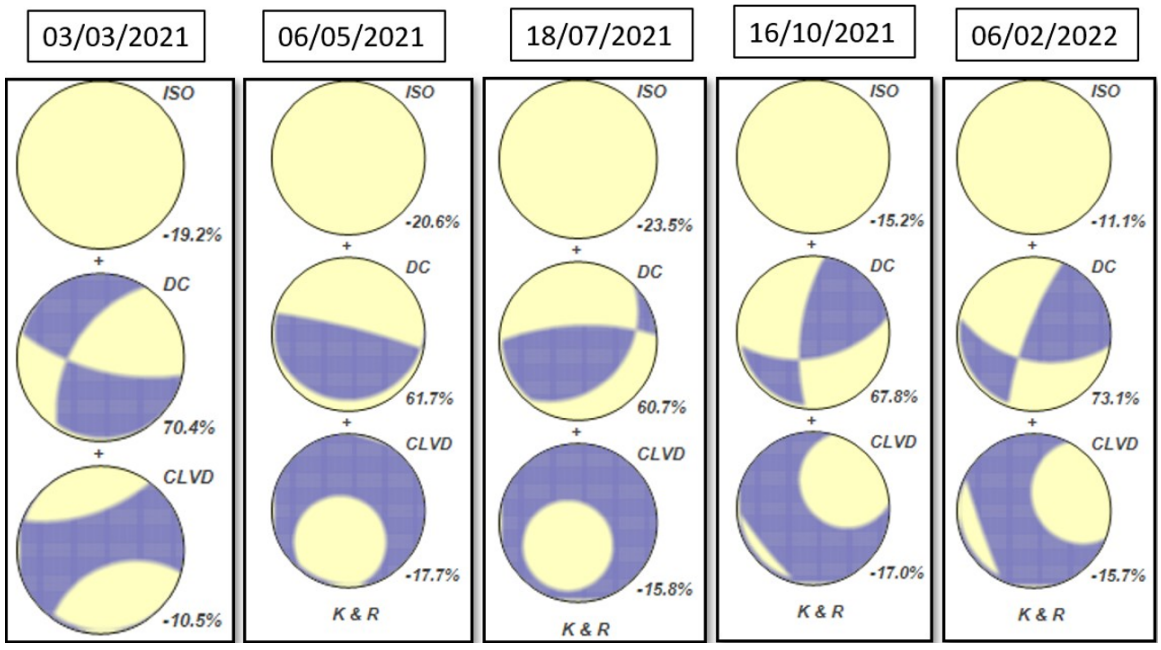

Figure 14 Focal mechanism solution beachballs of the analysed events, representing the isotropic (ISO), double-couple (DC) and compensated linear vector dipole (CLVD) tensors, respectively

The uncertainty of the results is determined using the normalised root mean square (RMS) and the condition number (CN) (Stierle et al. 2014; Kwiatek et al. 2016; Gnyp & Malytskyy 2021; Dahm & Krüger 2014). Table 5

shows RMSERROR and CN values for the five analysed events. The results of the uncertainty measures are considered satisfactory for the events on 3 March 2021 and 6 February 2022, where both RMSERROR and CN are relatively low. However, the increase in the CN for the other three events indicates lower confidence in the solution which can be attributed to numerous factors including data noise, and inaccurate velocity model and sensor coverage, which are prevalent issues in mining seismology (Scognamiglio et al. 2016; Zhang et al. 2016; Vavryčuk 2015; Caputa et al. 2015).

Table 5 RMSERROR and condition number (CN) values of the resultant solution for the five studied events

Event	RMSERROR	CN
03/03/2021	0.232	33
06/05/2021	0.383	46
18/07/2021	0.222	46
16/10/2021	0.215	51
06/02/2022	0.113	18

6 Conclusion

The present study reports the analysis results of induced seismicity in the lower zone of YD mine. A mine-wide numerical model is constructed in finite difference software FLAC3D by considering the three mining zones (upper, middle and lower) along with the diabase dykes, and calibrated based on in situ stress measurements. A step-by-step investigation is conducted to assess seismicity using Hoek–Brown compressive SF, BSR and BPI. Comparison with seismic source location, magnitude and mechanisms is presented. The modelling results show that as mining proceeds, BSR values at large event locations reach the damage initiation threshold. BSR values of two large seismic events exceeding the failure limit of 0.7, indicating strong brittle failure potentials. BPI values show better correlation with four events and are found to reach above 100% with mining advance. Increased BPI values signify more energy being stored in the rock, which increases the risk of local failure with future mining operations. The SF criterion has an even better correlation with the occurrence of large events since five events have SF values that are less than one. As a continuum model, FLAC3D treats the rock mass as a homogeneous, isotropic material and does not explicitly model discontinuities. The stress concentration that typically develops at the contact surface between rock blocks results in the sudden release of energy in the form of shear slip. Such hypothesis is confirmed by the results of MT analysis where the DC component is about 70%. Thus for future research, considering modelling of the fracture network that consists of the main discontinuity sets in the large seismic event locations could yield more accurate representations of the studied indicators. Such a hybrid approach would still require a FLAC3D model to obtain the field stress in the area to be further discretised with discrete element modelling approaches. The generated focal mechanism solutions suggest that shear failure is dominant in the sources with implosive deformation. The source mechanisms of the analysed events are most likely shearing failure/compressional failure, which is in line with the continuum modelling results.

Acknowledgement

The authors would like to acknowledge Mitacs for its financial support of this project, and are grateful to Alamos Gold Inc. for the data provided by the YD mine.

References

Alamos Gold Inc. 2020, *Ground Control Management Plan*.

Brune, J 1971, 'Correction [to "Tectonic stress and the spectra, of seismic shear waves from earthquakes"]', *Journal of Geophysical Research*, vol. 76, no. 20, pp. 5002.

Brune, N 1970, 'Tectonic stress and the spectra of seismic shear waves from earthquakes', *Journal of Geophysical Research*, vol. 75, no. 26, pp. 4997–5009.

Caputa, A, Rudziński, Ł & Cesca, S 2021, 'How to assess the moment tensor inversion resolution for mining induced seismicity: a case study for the Rudna mine, Poland', *Frontiers in Earth Science*, vol. 9, 671207.

Caputa, A, Talaga, A & Rudziński, Ł 2015, 'Analysis of post-blasting source mechanisms of mininginduced seismic events in Rudna copper mine, Poland', Contemporary Trends in Geoscience, 4.

Castro, LA, Bewick, RP & Carter, TG 2012, 'An overview of numerical modelling applied to deep mining', *Innovative Numerical Modelling in Geomechanics*, CRC Press, Boca Raton, pp. 393-414.

Chen, J, Liu, X & Xu, Q 2017, 'Numerical simulation analysis of damage mode of concrete gravity dam under close-in explosion', *KSCE Journal of Civil Engineering*, vol. 21, pp. 397–407.

Cronin, V 2004, 'A draft primer on focal mechanism solutions for geologists', Baylor University, Texas.

Dahm, T & Krüger, F 2014, 'Moment tensor inversion and moment tensor interpretation', in P Bormann (ed.), *New Manual of Seismological Observatory*, Deutsches, GeoForschungsZentrum GFZ, Potsdam.

Eaton, DW 2008, 'Microseismic focal mechanisms: a tutorial', *CREWES Research Report*, 20, pp. 1–11.

ESG Solutions 2020, *Seismic Software Suite (HSS)*, computer software, https://www.environmental-expert.com/software/esg-windows-based-hyperion-seismic-software-suite-hss-605490.

Eyre, TS & van der Baan, M 2015, 'Overview of moment-tensor inversion of microseismic events', *The Leading Edge*, vol. 34, no. 8, pp. 882–888.

Gnyp, A & Malytskyy, D 2021, 'Differential and source term's locations of the 2015 Teresva (East Carpathians) series and their tectonic implications', *Acta Geophysica*, vol. 69, no. 6, pp. 2099–2112.

Heidarzadeh, S, Saeidi, A & Rouleau, A 2019, 'Evaluation of the effect of geometrical parameters on stope probability of failure in the open stoping method using numerical modeling', *International Journal of Mining Science and Technology*, vol. 29, no. 3, pp. 399–408.

Heidarzadeh, S, Saeidi, A & Rouleau, A 2020, 'Use of probabilistic numerical modeling to evaluate the effect of geomechanical parameter variability on the probability of open-stope failure: a case study of the Niobec Mine, Quebec (Canada)', *Rock Mechanics and Rock Engineering*, vol. 53, pp. 1411–1431.

Hoek, E, Carranza-Torres, C & Corkum, B 2002, 'Hoek-Brown failure criterion-2002 edition', *Proceedings of NARMS-Tac 2002*, pp. 267–273.

ITASCA, F 2009, *Fast Lagrangian Analysis of Continua in 3 Dimensions*, version 4.0, computer software.

ITASCA, F 2013, *Fast Lagrangian Analysis of Continua in 3 Dimensions*, online manual, pp. 175–180.

Julian, BR, Miller, AD & Foulger, GR 1998, 'Non-double-couple earthquakes 1. Theory', *Reviews of Geophysics*, vol. 36, no. 4, pp. 525–549.

Khalil, H 2023, *Effect of Mining and Geology on Induced Seismicity - A Case Study*, Masters thesis, McGill University, Montreal.

Khalil, H, Chen, T, Xu, Y H & Mitri, H 2022, 'Effect of mining and geology on mining-induced seismicity–A case study', *Journal of Sustainable Mining*, vol. 21, no. 3, pp. 200–215.

Knopoff, L & Randall, MJ 1970, 'The compensated linear-vector dipole: a possible mechanism for deep earthquakes', *Journal of Geophysical Research*, vol. 75, no. 26, pp. 4957–4963.

Kwiatek, G, Martínez-Garzón, P & Bohnhoff, M 2016, 'HybridMT: A MATLAB/shell environment package for seismic moment tensor inversion and refinement', *Seismological Research Letters*, vol. 87, no. 4, pp. 964–976.

Li, T, Cai, MF & Cai, M 2007, 'A review of mining-induced seismicity in China', *International Journal of Rock Mechanics and Mining Sciences*, vol. 44, no. 8, pp. 1149–1171.

Li, Y 2021, *Determination of Mining-Induced Stresses Using Diametrical Rock Core Deformation Measurement and Finite Element Modelling*, master's thesis, McGill University, Montreal.

Li, Y, Chen, T, Blake, T & Mitri, HS 2024, 'Validation of diametrical core deformation technique for mining-induced stress estimation: a case study', *Rock Mechanics and Rock Engineering*, pp. 1–10, http://dx.doi.org/10.1007/s00603-024-03866-x

Li, Y & Mitri, HS 2022, 'Determination of mining-induced stresses using diametral rock core deformations', *International Journal of Coal Science & Technology*, vol. 9, no. 1.

Lizurek, G & Wiejacz, P 2011, 'Moment tensor solution and physical parameters of selected recent seismic events at Rudna copper mine', *Geophysics in Mining and Environmental Protection*, pp. 11–19, http://dx.doi.org/10.1007/978-3-642-19097-1_2

Ma, J, Dong, L, Zhao, G & Li, X 2019, 'Focal mechanism of mining-induced seismicity in fault zones: a case study of Yongshaba mine in China', *Rock Mechanics and Rock Engineering*, vol. 52, no. 9, pp. 3341–3352.

Malovichko, D, van Aswegen, G & Clark, R 2012, 'Mechanisms of large seismic events in platinum mines of the Bushveld Complex (South Africa)', *Journal of the Southern African Institute of Mining and Metallurgy*, vol. 112, no. 6, pp. 419–429.

McGarr, A 1992, 'Moment tensors of ten Witwatersrand mine tremors', *Pure and Applied Geophysics*, vol. 139, pp. 781–800.

McKinnon, SD & Labrie, D 2006, 'Interpretation of stresses adjacent to the Cadillac Fault assuming marginal large-scale rock mass stability', *Proceedings of the International Symposium on In-situ Rock Stresses*, A.A. Balkema, Rotterdam, pp. 409–417.

MDEng 2017, *Geomechanical Review of Young-Davidson Life of Mine Extraction Plan*, Mine Design Engineering Report #1015-R1606-01.

Mitri, H, Tang, B & Vicenzi, I 2000, 'Modeling of tunnel face stresses in bedded rock', *The 53rd Canadian Geotechnical Conference*, Canadian Geotechnical Society, Montreal.

Mitri, HS, Tang, B & Simon, R 1999, 'FE modelling of mining-induced energy release and storage rates', *Journal of the Southern African Institute of Mining and Metallurgy*, vol. 99, no. 2, pp. 103–110.

Ren, Y, Vavryčuk, V, Wu, S & Gao, Y 2021, 'Accurate moment tensor inversion of acoustic emissions and its application to Brazilian splitting test', *International Journal of Rock Mechanics and Mining Sciences*, vol. 141, 104707.

Sainoki, A, Schwartzkopff, AK, Jiang, L & Mitri, HS 2021, 'Numerical modeling of complex stress state in a fault damage zone and its implication on near-fault seismic activity', *Journal of Geophysical Research: Solid Earth*, vol. 126, no. 7, e2021JB021784.

Scognamiglio, L, Magnoni, F, Tinti, E & Casarotti, E 2016, 'Uncertainty estimations for moment tensor inversions: the issue of the 2012 May 20 Emilia earthquake', *Geophysical Journal International*, vol. 206, no. 2, pp. 792–806.

Shnorhokian, S, Mitri, HS & Moreau-Verlaan, L 2015, 'Stability assessment of stope sequence scenarios in a diminishing ore pillar', *International Journal of Rock Mechanics and Mining Sciences*, vol. 74, pp. 103–118.

Šílený, J & Milev, A 2008, 'Source mechanism of mining induced seismic events—resolution of double couple and non-double couple models', *Tectonophysics*, vol. 456, no. 1-2, pp. 3–15.

Stec, K & Drzewiecki, J 2012, 'Mine tremor focal mechanism: an essential element for recognising the process of mine working destruction', *Acta Geophysica*, vol. 60, pp. 449–471.

Stein, S & Wysession, M 2009, 'An introduction to seismology, earthquakes, and earth structure', John Wiley & Sons, Hoboken.

Stierle, E, Vavryčuk, V, Šílený, J & Bohnhoff, M 2014, 'Resolution of non-double-couple components in the seismic moment tensor using regional networks—I: a synthetic case study', *Geophysical Journal International*, vol. 196, no. 3, pp. 1869–1877.

Tierney, S 2019, *Moment Tensors – A Practical Guide*, blog post, https://mxrap.com/2019/07/26/moment-tensors-a-practical-guide/

Vavryčuk, V 2015, 'Moment tensor decompositions revisited', *Journal of Seismology*, vol. 19, no. 1, pp. 231–252.

Vennes, I, Mitri, H, Chinnasane, DR & Yao, M 2020, 'Large-scale destress blasting for seismicity control in hard rock mines: a case study', *International Journal of Mining Science and Technology*, vol. 30, no. 2, pp. 141–149.

Yang, J, Lu, W, Hu, Y, Chen, M & Yan, P 2015, 'Numerical simulation of rock mass damage evolution during deep-buried tunnel excavation by drill and blast', *Rock Mechanics and Rock Engineering*, vol. 48, pp. 2045–2059.

Zhang, H, Eaton, DW, Li, G, Liu, Y & Harrington, RM 2016, 'Discriminating induced seismicity from natural earthquakes using moment tensors and source spectra', *Journal of Geophysical Research: Solid Earth*, vol. 121, no. 2, pp. 972–993.